AGU PUBLICATIONS

JGR

Journal of Geophysical Research: Space Physics

RESEARCH ARTICLE
10.1002/2015JA022261

Key Points:
- Determined the ion composition and spatial variations for 5.9 <= L < 9.5 region
- Using CODIF/Cluster observations
- Results indicate a localized enhancement of heavy ions due to high-latitude ionospheric outflows

Supporting Information:
- Supporting Information S1
- Figure S1
- Figure S2
- Figure S3

Correspondence to:
J. K. Sandhu,
js423@le.ac.uk

Citation:
Sandhu, J. K., T. K. Yeoman, R. C. Fear, and I. Dandouras (2016), A statistical study of magnetospheric ion composition along the geomagnetic field using the Cluster spacecraft for L values between 5.9 and 9.5, *J. Geophys. Res. Space Physics*, *121*, 2194–2208, doi:10.1002/2015JA022261.

Received 11 DEC 2015
Accepted 18 FEB 2016
Accepted article online 23 FEB 2016
Published online 18 MAR 2016
Corrected 20 JUN 2016

This article was corrected on 20 JUN 2016. See the end of the full text for details.

A statistical study of magnetospheric ion composition along the geomagnetic field using the Cluster spacecraft for L values between 5.9 and 9.5

J. K. Sandhu[1], T. K. Yeoman[1], R. C. Fear[1,2], and I. Dandouras [3,4]

[1]Department of Physics and Astronomy, University of Leicester, Leicester, UK, [2]Now at Department of Physics and Astronomy, University of Southampton, Southampton, UK, [3]University of Toulouse, UPS-OMP, Institut de Recherche en Astrophysique et Planétologie, Toulouse, France, [4]CNRS, IRAP, Toulouse, France

Abstract Using ion density data obtained by the CODIF (ion Composition and Distribution Function analyser) instrument on board the Cluster spacecraft, for the interval spanning 2001–2005, an empirical model describing the average ion mass distribution along closed geomagnetic field lines is determined. The empirical model describes the region spanning $5.9 \leq L < 9.5$, with dependences on L shell and magnetic local time included, and represents ions in the energy range of 0.025 to 40 keV/charge. The data reduction process involves the identification and rejection of CODIF data contaminated by penetrating energetic radiation belt particles, found to frequently occur for $L < 5.9$. Furthermore, a comparison of data with observations of the cold plasma population in the region provides evidence that the CODIF data set is representative of the full plasma population. The variations in average ion mass along the field lines were modeled using a power law form, which maximizes toward the magnetic equatorial plane, with observed power law index values ranging between approximately −2.0 and 0.0. The resulting model illustrates some key features of the average ion mass spatial distribution, such as an average ion mass enhancement at low L in the evening sector, indicating the transport of high-latitude heavy ion outflows to the closed inner magnetosphere.

1. Introduction

Variations in magnetospheric plasma mass density provide information on the morphology of the magnetosphere and the different dynamical processes occurring. For example, the magnetospheric mass density plays a crucial role in determining the propagation of wave modes implicated in radiation belt energization and decay [*Meredith et al.*, 2003; *O'Brien et al.*, 2003]. In addition, the magnetospheric mass density is a significant factor in influencing dayside reconnection rates [*Borovsky and Denton*, 2006], and therefore has implications for the coupling of the solar wind to the magnetosphere. An important application for models of the magnetospheric mass density is in determining the frequencies of magnetospheric ultralow-frequency waves and, hence, the response time of the magnetosphere to perturbations. As well as varying with changes in the number density of the electrons and ions, the ion composition contributes significantly to the plasma mass density. Therefore, it is of scientific interest to understand the plasma ion composition and its spatial variations.

The plasma populating Earth's magnetosphere has two sources. Entry of the solar wind into the magnetosphere supplies light ions (H^+ and He^{++}), whereas plasma of ionospheric origin has a different composition. Observations show that although ionospheric plasma consists predominantly of H^+ ions, an enhanced supply of heavy ions, in particular O^+, can occur [*Shelley et al.*, 1972, 1982; *Lockwood et al.*, 1985; *Chappell et al.*, 1987; *Andre and Yau*, 1997; *Yau and Andre*, 1997; *Haaland et al.*, 2013]. The heavy ion loading of the magnetosphere depends on a range of dynamical processes resulting in the transport of heavy ions to the closed inner magnetosphere, and at times, the presence of O^+ ions can represent a significant proportion of the magnetospheric plasma [*Chappell*, 1982; *Young et al.*, 1982; *Horwitz et al.*, 1984, 1986; *Roberts et al.*, 1987; *Comfort et al.*, 1988; *Andre and Yau*, 1997; *Yau and Andre*, 1997; *Moore et al.*, 1999; *Winglee*, 2000; *Korth et al.*, 2002; *Kistler et al.*, 2006; *Howarth and Yau*, 2008; *Haaland et al.*, 2009; *Liao et al.*, 2010; *Nosé et al.*, 2011; *Haaland et al.*, 2012a, 2012b; *Li et al.*, 2012; *Slapak et al.*, 2012; *Nosé et al.*, 2015]. This study aims to use direct observations of ion composition to determine an empirical model of how the average ion mass is distributed in the closed magnetosphere, in a region covering the outer heavy ion torus, plasmatrough, and near-Earth plasma sheet, considering both variations in the equatorial plane and the distribution of average ion mass along magnetic field lines.

Multiple studies examining the ion composition in the closed magnetosphere exist, although they are not without limitations. Many studies examine ion composition using measurements of the O^+/H^+ density ratio, representing the concentration of heavy ions in the plasma [*Mouikis et al.*, 2010; *Ohtani et al.*, 2011; *Lee and Angelopoulos*, 2014; *Maggiolo and Kistler*, 2014]. *Mouikis et al.* [2010] examined the spatial distribution of the O^+/H^+ density ratio, using Cluster CODIF (ion Composition and Distribution Function analyser) measurements taken close to the equatorial plane. The data covered radial distances from 15 to 19R_E, in the plasma sheet region. The analysis provided information on the magnetic local time (MLT) variations in the ion composition; however, the dependences were not quantified and variations with *L* shell were not considered. *Maggiolo and Kistler* [2014] also used Cluster CODIF data to produce statistical maps showing the O^+/H^+ density ratio in the equatorial plane. The measurements were constrained to plasma corresponding to an observed isotropic distribution, allowing mapping along the field lines, considering the near-Earth plasma sheet population within radial distances of 7 to 8R_E, as well as in the midtail region (15 to 20R_E). Other data sets have also been employed to examine the spatial distribution of the O^+/H^+ density ratio in the equatorial plane. *Ohtani et al.* [2011] presented Geotail EPIC (Energetic Particle and Ion Composition) observations for the plasma sheet covering radial distances from 5 to 32R_E, and *Lee and Angelopoulos* [2014] used THEMIS (Time History of Events and Macroscale Interactions during Substorms) data over *L* shells from approximately 6 to 12. However, these studies are restricted to observations describing the equatorial distribution and do not consider variations along magnetic field lines, which can provide some important information concerning the transport of heavy ions to the closed magnetosphere. A study conducted by *Denton et al.* [2009] used an indirect technique to observe the distribution of average ion mass along the field lines. Using measurements of multiharmonic toroidal Alfvén wave frequencies, obtained by the Cluster spacecraft, the distributions of mass density, ρ, and electron density, n_e, were obtained, which provided a distribution of average ion mass (ρ/n_e) along the field lines. This technique was applied to only two case studies, as opposed to a statistical study. Furthermore, the inversion technique utilized to indirectly estimate the mass density makes several simplifying approximations and requires functional forms for the dependences along the field lines to be assumed.

A survey of existing work indicates that there are no empirical models providing a description of the average ion mass spatial distribution. An advantage of considering average ion mass, as opposed to the O^+/H^+ density ratio, is that the contribution to determining the total plasma mass density can be clearly interpreted, and influences from other ion species are also included. Observations have shown that He^+ can also constitute a significant proportion of the magnetospheric population at times, affecting the ion composition [*Yamauchi et al.*, 2014a]. By using a large data set, providing statistically significant results with good spatial coverage, this study presents an empirical model detailing the distribution of average ion mass along the field lines, including dependences with *L* shell and MLT.

2. Instrumentation and Data Reduction

Data are obtained from the four identical Cluster spacecraft (C1, C2, C3, and C4), which are arranged in a tetrahedral configuration. The polar orbits of the spacecraft cross many key regions of the magnetosphere (see *Escoubet et al.* [1997] for further details) and so provide the necessary data coverage required for this study. The data set used, obtained from the CSA (Cluster Science Archive), covers the time interval of 2001–2005.

This study uses data from the CIS (Cluster Ion Spectrometry) experiment [*Rème et al.*, 1997]. This includes the CODIF instrument (ion Composition and Distribution Function analyser), which is a high-sensitivity, mass-resolving spectrometer measuring the full three-dimensional distribution functions of the key ion species in the energy range 0.025–40 keV/charge. Integrals of the resulting distribution function, with a time resolution of one spacecraft spin (4s), allow the ion density to be calculated for each of the ion species, specifically H^+, O^+, and He^+. Although the CODIF instrument also measures the distributions functions of He^{++} ions, these are omitted from the data set, as He^{++} density data are overestimated due to strong contamination by H^+ ions. Using the densities, n_i, with the atomic mass, m_i, of each ion, *i*, the average ion mass, m_{av}, can be estimated from

$$m_{av} = \frac{\sum_i \left(n_i m_i\right)}{\sum_i n_i} \tag{1}$$

The ground calculated moments of the CODIF HS (High Sensitivity) data, limited to the MAG (Magnetosphere) modes, as appropriate for the outer plasmasphere and plasmatrough regions, provide the ion density measurements. From this data set, the inferred average ion mass measurements are obtained over the required

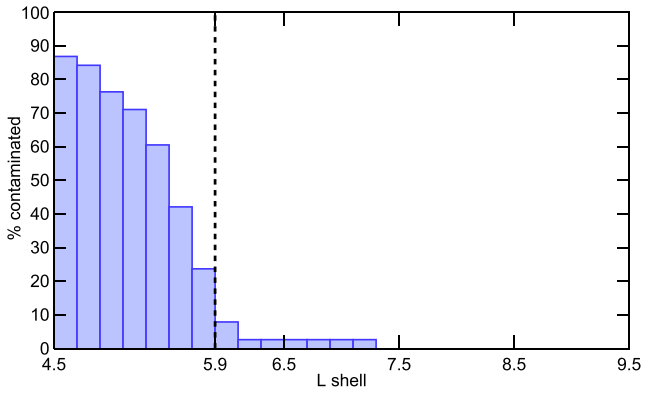

Figure 1. Histogram showing the percentage of cases where contaminated CODIF measurements, due to energetic radiation belt particles, were observed as a function of *L* shell. This is based on a representative sample of 38 passes through the radiation belt region. The vertical dashed line at $L = 5.9$ indicates the lower *L* shell boundary of CODIF data used in this study.

time interval, although it should be noted that data from the Cluster spacecraft C2 and C3 are not used (the CIS instrument is nonoperational on C2, and there are instrumental issues with the CODIF sensor on C3).

An important aspect concerning the CODIF data set that should be considered is the background contamination of the measurements due to penetrating energetic radiation belt particles. Although the effects of the background contamination are reduced due to the time-of-flight method of analysis used by CODIF, a visual inspection of the energy-time spectrograms indicates that the occurrence of data contamination is not negligible. Furthermore, the background contamination effect is mass dependent, such that it is stronger for the O^+ ions [*Mouikis et al.*, 2014]. This results in overestimated O^+ densities, and therefore overestimated average ion mass values, for observations with significant background contamination. Further details on the effect of the penetrating radiation belt particles on the CODIF measurements are described by *Ganushkina et al.* [2011], *Kronberg et al.* [2012], and *Mouikis et al.* [2014]. In order to identify where the CODIF data are significantly affected by the background contamination, a sample of representative passes through the radiation belt regions was assessed for signatures of contamination. This sample consisted of 38 passes in total, for a range of different seasons and orbit configurations. Figure 1 shows the frequency of contamination of the CODIF data in this sample as a function of the spacecraft *L* value. It is clearly apparent that the contamination of data occurs more frequently at lower *L* values, where the spacecraft is more likely to encounter the radiation belts and the radiation belt particles are more energetic. Based on the inspection of the sample spacecraft passes, CODIF data obtained by the spacecraft at *L* values below 5.9 are not used in this study, due to the high occurrence of background contamination. Data obtained at $L \geq 5.9$ are less likely to be contaminated. For example, within the range $5.9 \leq L < 6.5$, on average 4% of the data in the sample is contaminated compared to an average of 64% for $4.5 \leq L < 5.9$. Therefore, restricting the CODIF data used to observations at *L* values at 5.9 or above will reduce the background contamination to a negligible effect.

2.1. Comparison to Retarding Potential Analyser Observations

In order to examine how representative the average ion mass data set is of the total plasma population in this region, the following analysis has been conducted. The CODIF instrument includes the RPA (Retarding Potential Analyser) device [*Rème et al.*, 1997]. When CODIF is operating in the RPA mode, ion densities in the energy range of 0.7–25 eV/charge (relative to the spacecraft potential) are provided. Therefore, densities measured using the RPA mode, and the corresponding calculated average ion mass, represent the cold population of plasma, which may be a significant population in this region. Figure 2 shows the correlation of ion density (n_i) observations and calculated average ion mass (m_{av0}) values for data obtained in the MAG modes, corresponding to higher energy particles (0.025–40 keV/charge), and the RPA mode, corresponding to lower energy particles (0.7–25 eV/charge). In total, 2419 values for the MAG modes and 236 values for the RPA modes are obtained over the full time interval, where the values correspond to data binned for position for each orbit and averaged (refer to section 2.2 for details on the binning). The data are binned for *L* shell, using a bin size of 0.1, and the *L* shell of each bin is indicated by the color of the point in Figure 2. Figures 2a–2c show the correlation of ion densities of the key ion species (H^+, O^+, and He^+, respectively) for the MAG mode and RPA mode of the CODIF instrument. It can be seen that the majority of the points in Figures 2a–2c lie below the

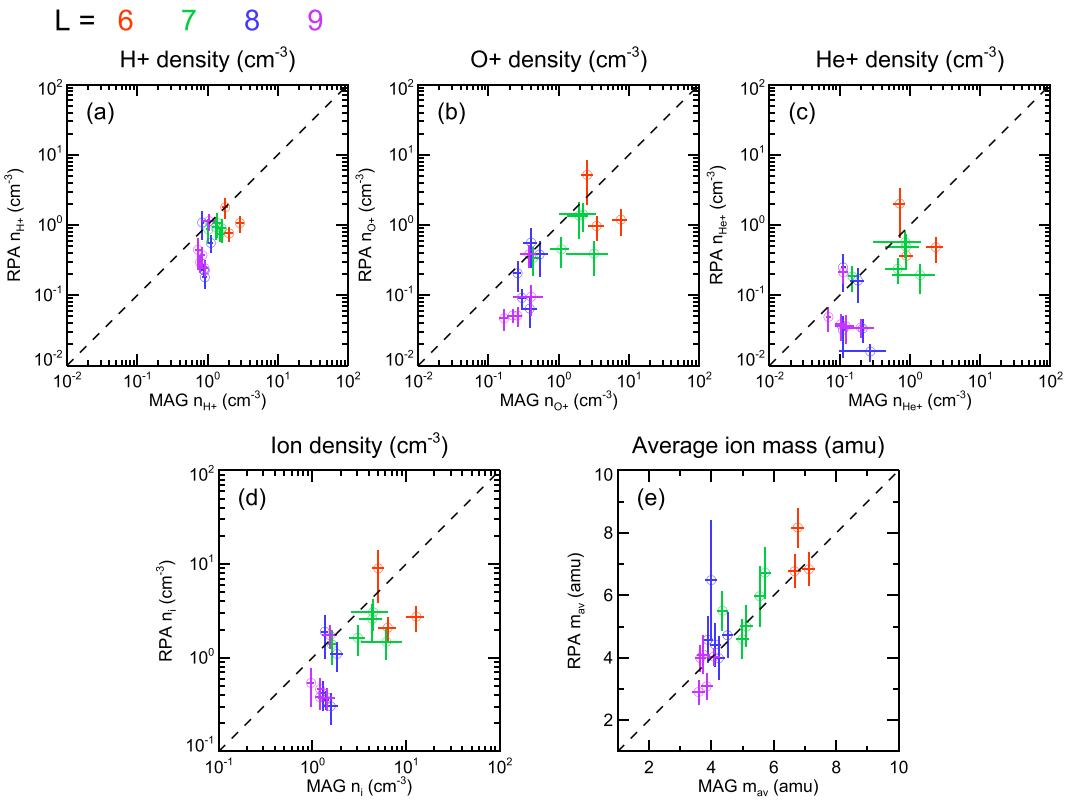

Figure 2. Plots showing correlations of CODIF measurements in the RPA (corresponding to 0.7–25 eV/charge energy range) and MAG (0.025–40 keV/charge energy range) modes. All data are binned for L value (represented by the color of the points), with a bin size of 0.1, and the horizontal and vertical bars on each point correspond to the statistical standard error of the data in the L value bin. The dashed lines in each panel indicate $y = x$. (a–c) Correlation of H^+, O^+, and He^+ ion densities, n_{H+}, n_{O+}, and n_{He+}, (cm^{-3}), respectively, measured by CODIF in the RPA and MAG modes. (d) Correlation of the total ion density, n_i, (cm^{-3}) measured by CODIF in the RPA and MAG modes. (e) Correlation of average ion mass, m_{av}, (amu) values calculated from CODIF measurements in the RPA and MAG modes.

$y = x$ line, indicating that the densities observed by the MAG mode are, in general, greater compared to the densities observed by the RPA mode. This feature is further demonstrated by Figure 2d, which shows the corresponding total ion densities (summed over all ion species) for the MAG and RPA modes. The total ion density is observed to be increased for the MAG mode, representing the higher energy population, in comparison with the observed total ion density for the RPA mode, which measures the cold population. This indicates that for the region considered here, the cold population, observed by the RPA mode of CODIF, is not the dominant population, and the hotter population, observed by the MAG mode, constitutes a larger proportion of the total plasma. This is not unexpected as the population observed by the RPA mode, at these L shells located predominantly outside of the plasmasphere, is generally considered to correspond mainly to detached plumes and is not typically a major component of the plasma in this region [*Dandouras et al.*, 2005; *Darrouzet et al.*, 2009]. On the other hand, the MAG mode observations generally represent the ring current, plasma sheet, and other energized populations [*Dandouras et al.*, 2009; *Yamauchi et al.*, 2014a, 2014b], a significant proportion of the plasma for the considered L shells. An analysis of case studies where the CODIF instrument on board one spacecraft was operating in MAG mode while the CODIF instrument on board another spacecraft was operating in RPA mode allowed a comparison of these two corresponding populations at approximately the same time. Although details are not shown here for all case studies, an example is now briefly highlighted to support the findings.

Figure 3 shows observations obtained by the CODIF instrument during a perigee pass through the dayside magnetosphere for the interval from 21:00 UT on 20 October 2002 to 02:00 UT on 21 October 2002. The CODIF instrument was operating in MAG mode for Cluster 1 (blue), observing ions in the energy range of 0.025–40 keV/charge. Conversely, the CODIF instrument on board Cluster 4 (red) was operating in RPA mode, where ion density observations correspond to the energy range of 0.7–25 eV/charge. Figure 3a shows the

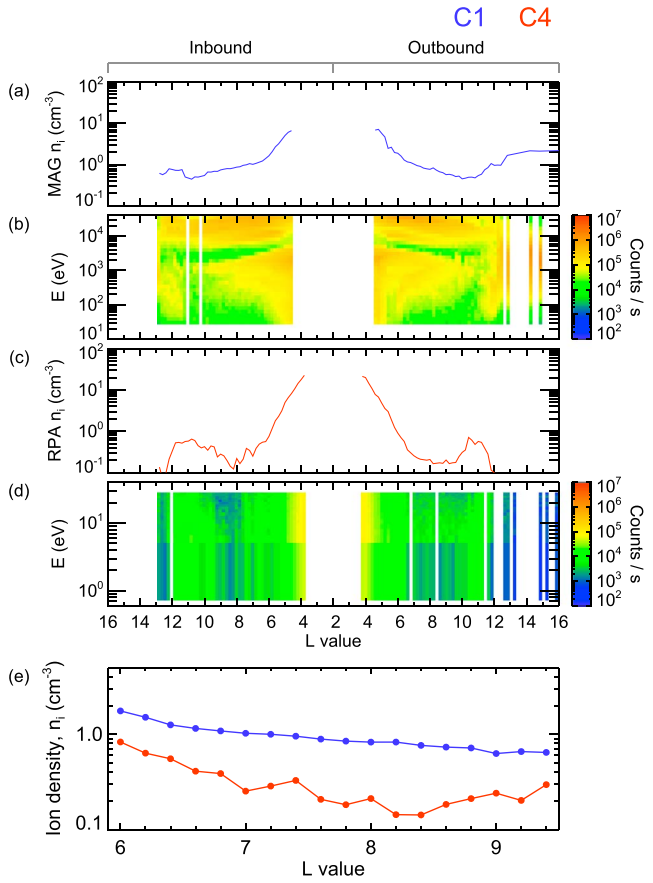

Figure 3. CODIF ion observations during a perigee pass for the interval from 21:00 UT on 20 October 2002 to 02:00 UT on 21 October 2002, for Cluster 1 (blue) and Cluster 4 (red). (a and b) The total ion density (n_i) and H^+ energy (E) spectrograms, respectively, observed by Cluster 1, where the CODIF instrument was operating in MAG mode. (c and d) The ion density and energy spectrograms, respectively, observed by Cluster 4, where the CODIF instrument was operating in RPA mode. Data in Figures 3a–3d are plotted as a function of L value, considering the inbound and outbound parts of the orbit separately, as labeled. Figure 3e shows the ion density variation with L, corresponding to the observations shown in Figures 3a and 3c for $5.9 \leq L < 9.5$, taking the inbound and outbound parts of the orbit together.

total ion density, n_i, and Figure 3b shows the H^+ ion energy spectrogram, where both are observed by Cluster 1 in the MAG mode. Figures 3c and 3d show the corresponding ion density and H^+ energy spectrogram, respectively, observed by Cluster 4 operating in RPA mode. The data have been binned for L value, using a bin size of 0.2, considering data from the inbound and outbound parts of the orbit separately. The observations in each bin are averaged and plotted as a function of L. A comparison of the energy spectrograms shown in Figures 3b and 3d appear to indicate that the cold population observed by the RPA mode is a continuation of the hot population observed by the MAG mode, with no separate cold population observed. This suggests that the cold and hot populations are of the same source. The corresponding spectrograms for He^+ ions and O^+ ions (not shown here) demonstrate the same feature. In order to directly compare ion density values for the L range of interest for this study, the observations shown in Figures 3a and 3c are shown in Figure 3e. Taking the inbound and outbound parts of the orbit together, the L profile is shown for an L range appropriate for the region considered by this study. The data have been binned for L value using a bin size of 0.2, and observations in each bin are averaged. It can be clearly seen that the ion densities corresponding to the MAG mode of the CODIF instrument (blue profile) are greater than the ion densities observed in the RPA mode (red profile), by a factor of ~2–6. For lower L values, outside of the range considered in Figure 3e, the low-energy ion densities are observed to dominate, as expected. However, this case study provides evidence that in the L range considered in this statistical study ($5.9 \leq L < 9.5$), the hotter ion population, observed by the MAG mode, is dominant relative to the colder ion population.

Overall, the total density observed by the MAG mode, with energies ranging between 0.025 and 40 keV/charge, is the major population for this region. Figure 2e demonstrates that the average ion mass values measured in the MAG mode can also be reasonably used to represent the cold population measured in the RPA mode. Figure 2e shows the correlation of average ion mass values calculated from ion density observations in the MAG mode with corresponding values in the RPA mode. It is clear from Figure 2e that across all L values shown, the points lie very close to the $y = x$ line. This indicates that the average ion mass values at lower energies, as measured by the RPA mode, are approximately equal to the average ion mass values measured in the MAG mode. Therefore, it appears that the ion composition of the plasma in the region examined is relatively uniform over the ion energies. This analysis has demonstrated that although CODIF is unable to observe some of the cold plasma population (due to spacecraft charging) and some of the hot plasma population (above the CODIF energy range), given the consistent values of average ion mass from the RPA mode energy range (0.7–25 eV/charge) and the MAG mode energy range (0.025–40 keV/charge), it is reasonable to consider that the average ion mass calculated from the MAG mode is generally representative of the total plasma population. It is important to recognize that there may be an additional cold plasma population in the plasma sheet at times, which cannot be observed due to spacecraft charging [*Seki et al.*, 2003]. Due to the instrumental limitations of the CODIF instrument, the possible existence of an additional cold plasma sheet population cannot be accounted for in this study.

2.2. Data Reduction

In order to examine the spatial variations in the average ion mass, the following technique is used. For each orbit, the data are binned by position into $0.5 \times 0.5 \times 0.5\ R_E$ bins, in the GSM (Geocentric Solar Magnetospheric) coordinate system. The average value and average time of measurement for the observations in each bin of the orbit is determined, where the number of observations that are averaged in a bin typically ranges between 10 and 100. From the position of each bin, the corresponding MLT can also be found. Over all orbits, the total number of passes through each bin is typically of the order 100.

The next step taken is to determine the L value for each position bin within each orbit, where the L value is the radial distance of the bin's field line in the magnetic equatorial plane. This is done by tracing the field line corresponding to the bin's position and average measurement time, as predicted by the T96 magnetic field model [*Tsyganenko*, 1996], and defining the T96 magnetic equatorial position as the point of maximum radial distance along the field line. However, for cases where the angular difference between the field line midpoint position and the point of maximum radial distance exceeds 10°, then the field line midpoint of the field line is used instead. This technique accounts for the highly compressed dayside field lines, and it should be noted that the critical angular difference of 10° has been empirically chosen from an analysis of a variety of field line configurations. The T96 magnetic field model is parametrized by the solar wind dynamic pressure, interplanetary magnetic field B_y and B_z components, and the *Dst* index. The parameter values corresponding to the average measurement time of each bin was obtained from the NASA/Goddard Space Flight Center OMNI data set through OMNIWeb, for the 1min averaged solar wind parameters, and from the World Data Center for Geomagnetism (Kyoto) data set, for hourly averaged *Dst* values.

The procedure of determining the L values for each position bin allows any points where the field line is traced as open by the T96 magnetic field model to be discarded, as this study is concerned only with the closed magnetosphere. However, there are inevitably some measurements on open field lines inaccurately modeled as closed field lines, which would contribute to some discrepancies in values taken near the magnetopause. In order to remove points corresponding to open field lines, a method adapted from *Clausen et al.* [2009] is employed, which will now be detailed. Figure 4 (first panel) shows an ion energy spectrogram obtained from CIS measurements using the HIA (Hot Ion Analyser) instrument [*Rème et al.*, 1997], which illustrates the change in ion populations during a portion of the C1 spacecraft orbit. The spacecraft passes from the cusp region, through the OCB (open-closed boundary), into the closed dayside magnetosphere, through perigee, and then into the northern cusp region via the OCB again. It is apparent that open field lines near the OCB are characterized by relatively high ion fluxes at approximately 0.2 keV energies (see Figure 4, fourth panel, for the DEF (differential energy flux) profile at 0.2 keV), which can be used to distinguish between open and closed field lines near the boundary. However, high ion fluxes at this energy range are also observed near perigee, which correspond to closed field lines, so the DEF profile of ions at 10.0 keV (Figure 4, third panel) is used to differentiate between these situations. This is done by identifying where the DEF of ions at 10.0 keV and 0.2 keV (Figure 4, third and fourth panels, respectively) exceed empirically defined critical values (dashed horizontal lines), which are indicated as red lines in the corresponding plots. From a comparison, points are defined as

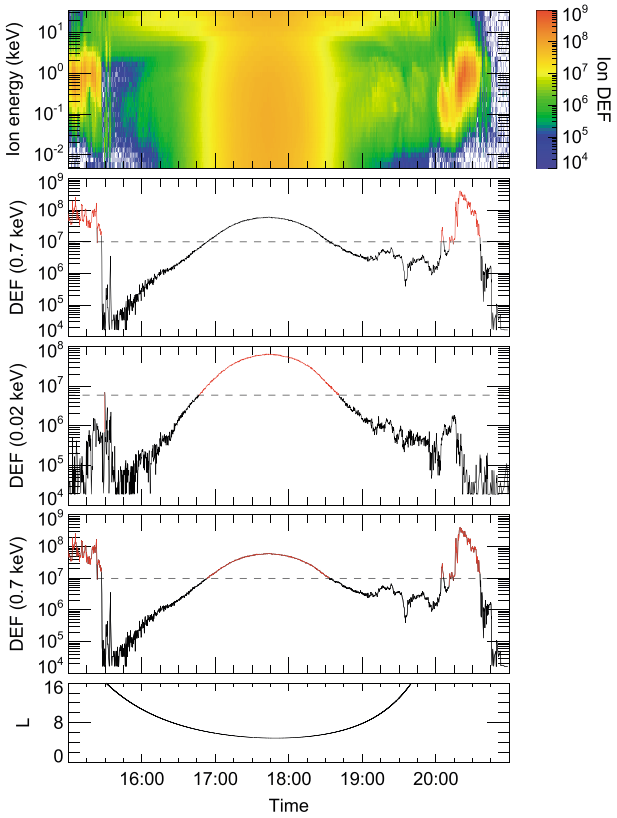

Figure 4. HIA/CIS ion energy flux data measured by C1 on 5 September 2002 (case study of *Clausen et al.* [2009]). (first panel) Ion energy flux spectrogram. (second panel) DEF (differential energy flux) profile for 0.2 keV ion energies, with the red line corresponding to field lines close to the magnetopause that have been identified as open. (third and fourth panels) DEF profiles corresponding to ion energies of 10.0 keV and 0.2 keV, respectively, where the red line indicates where the values exceed a threshold (indicated by horizontal dashed lines). (fifth panel) *L* values of the spacecraft position.

being on closed field lines if they have a DEF of ions at 0.2 keV below the critical value of 1×10^7 keV cm^{-2} s^{-1} sr^{-1} keV^{-1} or a DEF of ions at 10.0 keV above 6×10^6 keV cm^{-2} s^{-1} sr^{-1} keV^{-1}, which is demonstrated in Figure 4 (second panel), where red (black) points correspond to open (closed) field line measurements. Therefore, using HIA/CIS ion energy flux measurements, it can be determined whether the spacecraft is situated on an open or closed field line, where DEF profiles at two energies are used to distinguish between flux peaks for open field lines and at perigee. This method is applied to all points in the data sets, discarding any points identified to be on open field lines, and the resulting data sets demonstrate a reduction in the fluctuation of values close to the OCB, as expected. It should be noted here that while *Clausen et al.* [2009] used data from the PEACE (Plasma Electron and Current Experiment) instrument on board the Cluster satellite, we opted to use data from the HIA/CIS instrument instead, as this provides better data coverage over the required interval.

The resulting average ion mass data set, binned for position with corresponding MLT and *L* values determined and all measurements corresponding to open field lines removed, is now examined. Variations with magnetic latitude and *L* value in the CODIF data set can be examined from the average ion mass distribution in the *X*-*Z* plane of the SM (Solar Magnetic) coordinate system. The SM coordinate system is characterized by the geomagnetic dipole axis aligned with the *Z* axis, whereas the GSM coordinate system is defined such that the dipole axis is in the *X*-*Z* plane. Therefore, the SM coordinate system is more appropriate for assessing variations with magnetic latitude and *L* value and is used in this case. A coordinate transformation is used to determine the position in the SM coordinate system corresponding to each bin's position in the GSM coordinate system, taking bins over each orbit individually. The distribution of average ion mass is shown in Figure 5a in the *X*-*Z* plane, with the color of each point representing the average value of the measurements at that position (note that all measurements are now averaged over the number of orbit passes through the position

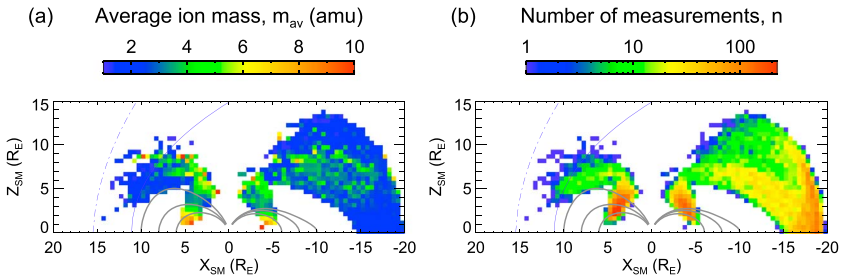

Figure 5. Spatial distribution of (a) average ion mass (amu) and (b) the number of measurements obtained by CODIF in the *X*-*Z* plane (SM coordinate system). The grey lines show reference T96 model magnetic field lines in the noon and midnight meridian planes, corresponding to spring equinox with a solar wind dynamic pressure of 2 nPa, for *L* values of 6, 8, and 10.

bin). The measurement positions have been azimuthally mapped into the noon-midnight meridian, such that the radial distance from the *Z* axis is represented as the magnitude of the *X* position and averaged separately over the dayside and nightside MLT sectors. All measurements in the Southern Hemisphere are also mapped to the corresponding position in the Northern Hemisphere, as it is assumed that the distribution along the geomagnetic field is symmetric about the magnetic equator. Note that spatial distributions of the data shown are binned with a bin size of 0.5 R_E.

In order to give an indication of the statistical significance of this spatial distribution, Figure 5b shows the equivalent spatial distribution of the number of measurements averaged over MLT in the *X*-*Z* SM plane. It can be seen that there are sufficient measurements in the data set to provide a reliable spatial distribution over a significant range of *L* shells. It is noted that the orbital coverage over each year for this time interval is similar, and therefore, solar cycle effects are not a significant systematic bias in coverage along the magnetic field lines.

3. Average Ion Mass Distribution Along the Magnetic Field

Using the average ion mass data set, the distribution along magnetic field lines can be examined, comparing data at different MLT and *L* values. This involves determining the most appropriate functional form to describe the distribution of average ion mass along the field lines. Then, using a least squares fitting method to determine the best fitting function parameters, a hierarchical modeling approach [*Clark and Gelfand*, 2006; *Tabachnick and Fidell*, 2006] is employed to define a model function that includes the dependences on *L* shell and MLT. As the function parameters vary on multiple levels (dependencies on the *L* shell of the field line and the MLT are expected), the hierarchical method separately fits to each of these levels. Therefore, the resulting best fit represents variations in the data set as a whole, as opposed to variations confined to one level.

The average ion mass data set, from measurements obtained by CODIF, provides sufficient spatial coverage along the field lines in the region spanning $5.9 \leq L < 9.5$. This corresponds to the outer heavy ion torus, plasmatrough, and near-Earth plasma sheet, which will be the region considered in the following analysis for the average ion mass distribution.

The average ion mass data are binned for the field line *L* value and the normalized radial distance along the field line, R_{norm}, which is the radial distance at which the measurement was obtained, $R\,(R_E)$, divided by the *L* value of the field line. The T96 magnetic field model is used here to determine the field line corresponding to each position bin, and the data are also binned for MLT (Magnetic Local Time) in order to further examine the spatial dependence.

An example plot showing the average ion mass as a function of normalized radius is shown in Figure 6 for an *L* shell of 7 (data are binned for *L* using a bin size of 1). Logarithmic scales have been used in Figure 6, in order to linearize power law dependences. Each point represents the average value in the bin, where the normalized radius bin width is equal to 0.05, and the color of the point corresponds to the number of averaged measurements in each bin, *n*. The vertical panels show the density data binned into 3h MLT intervals. The distribution of average ion mass values in each bin is indicated by the vertical grey line showing the range between the lower and upper quartile, with the short horizontal line representing the median value. As the profiles are smoothed using a boxcar function, with a width of three bins, some points are shifted relative to

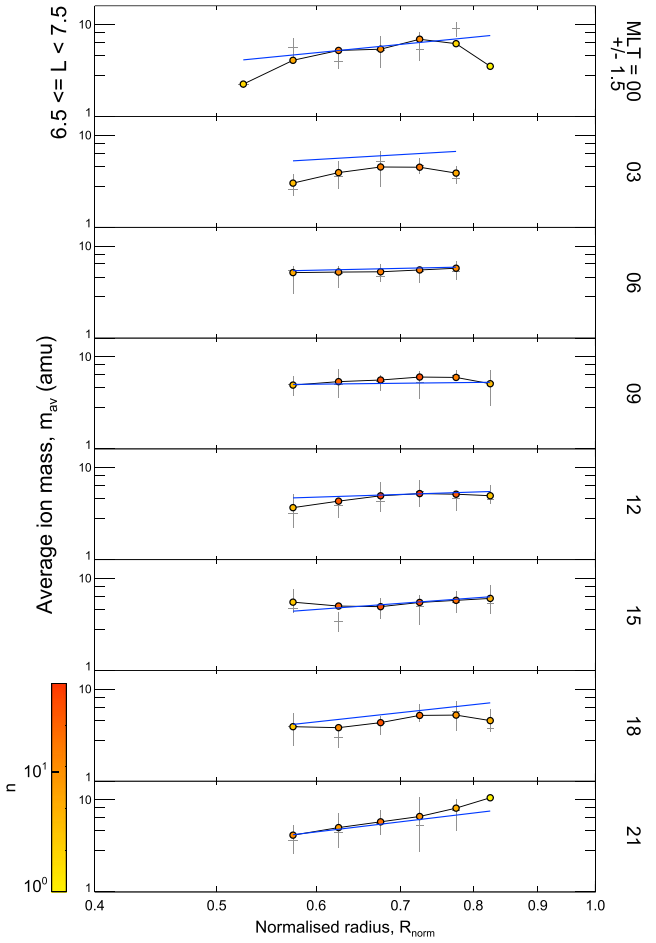

Figure 6. Average ion mass, m_{av} (amu), plotted as a function of normalized radius, R_{norm}, for $6.5 \leq L < 7.5$ at 3h MLT intervals, where the color of each point indicates the number of CODIF measurements, n, averaged in each bin. Note that a single CODIF measurement corresponds to an average of observations through a given position bin for one orbit. The upper and lower quartiles of the distribution of points averaged in each bin is shown by the grey line, intersected by a short horizontal line at the median value. The blue line represents the best fitting power law dependence.

the grey lines. It can be seen from the example in Figure 6 that the average ion mass tends to maximize toward the magnetic equator and decreases off equator, in agreement with results of previous studies [*Takahashi et al.*, 2004; *Denton et al.*, 2006].

To describe this dependence along the field line, a power law form is chosen, as shown in equation (2a):

$$m_{av} = m_{av0} R_{norm}{}^{-\beta} \tag{2a}$$

$$m_{av0} = 16.4 - 1.32L + (7.12 - 0.665L)\cos(15\text{MLT} + 32) \tag{2b}$$

$$\beta = -2.13 + 0.223L + (2.26 - 0.218L)\cos(15\text{MLT} + 219) \tag{2c}$$

where m_{av0} is the average ion mass at the magnetic equatorial point of the field line and β is the power law index. The power law index, β, is required to be negative, which results in a distribution where the average ion mass is a maximum at the magnetic equator and decreases toward the ionospheric ends of the magnetic field lines, as desired.

Using a least squares fitting method, weighted by the number of measurements in each bin, the best fit parameters (m_{av0} and β) are determined for each field line distribution. Variations in the best fit parameters are then quantified to include dependences with L and MLT, providing a hierarchical model for a power law field line distribution. The resulting power law model (equation (2a), with model parameters given by equations (2b) and (2c)) is shown as the solid blue line in Figure 6. Although some MLT sectors do not appear

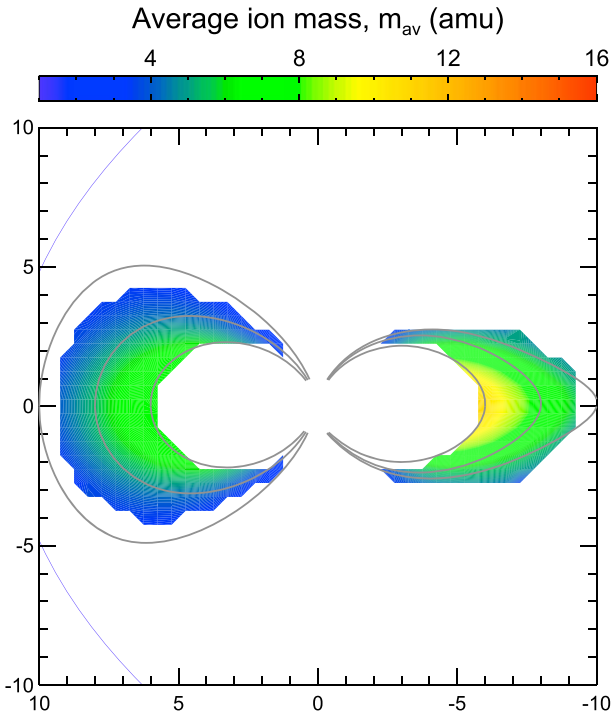

Figure 7. Spatial distribution in the *X-Z* SM plane using the average ion mass model. Note that the scales have been adjusted relative to the data plot (Figure 5) to focus on the most relevant regions. The grey lines show reference magnetic field lines in the noon and midnight meridian planes, for *L* values of 6, 8, and 10. The T96 magnetic field model used in this case corresponds to spring equinox, with a solar wind dynamic pressure of 2 nPa.

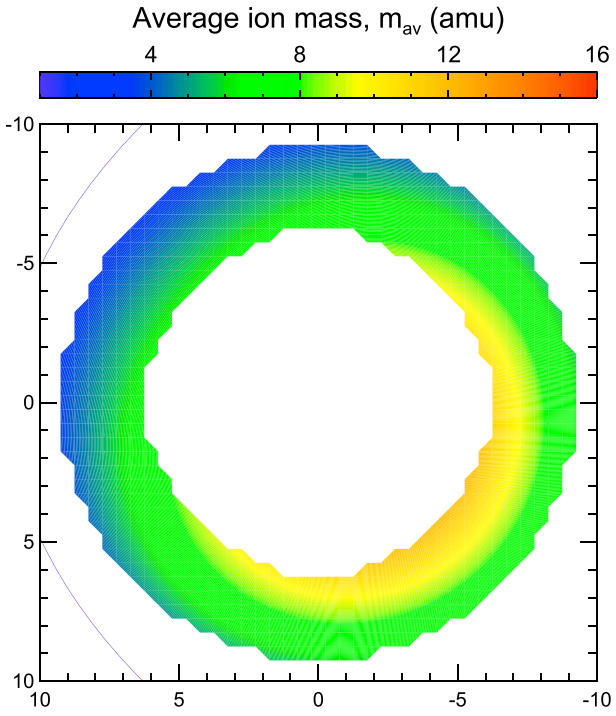

Figure 8. The spatial distribution of average ion mass in the T96 magnetic equatorial plane, in the same format as Figure 7.

to represent the best fit with minimum deviations from the data (e.g., Figure 6, second panel), this is due to the hierarchical technique employed. As mentioned previously, the model fits shown are results of fits at multiple levels, accounting for variations with L and MLT as well as R_{norm}.

The functions used for all model parameters are chosen to include a sinusoidal term, so that the circular form describes the MLT dependence. The phase term of the sinusoidal component indicates the location of the peak of the parameter in degrees of MLT eastward from the midnight meridian, and an amplitude term is included to determine the magnitude of the MLT dependence. Both the phase and amplitude terms are linear functions of L. An offset, which is also a linear function of L, is added to the sinusoidal term, to represent the mean value of the parameter across all MLT. The functional forms chosen to represent the MLT and L dependences have been chosen as they were the simplest forms that described the observed variations in the data, minimizing the number of free parameters. Note that when fitting for the model parameters, if no clear L dependence in the data was observed, the L dependence was removed from the relevant functional form. The key features of the parameters, and the variations with L and MLT, are discussed in further detail in section 4.

Equation (2), representing the average ion mass distribution along magnetic field lines, is used to examine the azimuthally mapped spatial distribution in the X-Z SM plane. This is shown in Figure 7. In addition, the spatial distribution in the T96 magnetic equatorial plane, predicted by the average ion mass model, is also shown in Figure 8.

4. Discussion

The empirical model for the average ion mass distribution along the field lines, presented in section 3, includes dependences on both L and MLT. The features apparent in the model will now be discussed in further detail, providing information on the processes influencing the heavy ion loading of field lines in the outer heavy ion torus, plasmatrough, and near-Earth plasma sheet regions of the closed magnetosphere.

The resulting variations along the field lines for average ion mass, presented in section 3, models the distribution to be a maximum toward the magnetic equator and decreasing off equator. Although there are no models (to our knowledge) describing the distribution of average ion mass along the geomagnetic field in quantitative detail, previous studies of the plasma mass density distribution along magnetic field lines suggest that the average ion mass should be locally peaked at the magnetic equator [*Takahashi et al.*, 2004; *Denton et al.*, 2006, 2009], in agreement with our field line distribution. The preferential concentration of heavy ions at the magnetic equatorial plane is expected due to the centrifugal force acting more effectively on heavier ions [*Denton et al.*, 2006, 2009], assuming similar temperatures for the ion species, and was described by *Lemaire and Gringauz* [1998] in terms of an effective gravitational potential well at the magnetic equator.

A key source of heavy ions in the region covered by the data set, determining the variations of the average ion mass distribution along the field line with L and MLT, is the plasma sheet population. It is known that enhanced ionospheric outflows of heavy ions occur in the cusp and nightside auroral regions [*Shelley et al.*, 1972, 1982; *Lockwood et al.*, 1985; *Chappell et al.*, 1987; *Chappell*, 1988; *Andre and Yau*, 1997; *Yau and Andre*, 1997; *Peterson et al.*, 2008; *Liao et al.*, 2010]. This plasma, which has an increased relative concentration of heavy ions, is convected into the plasma sheet and then earthward, populating the closed magnetosphere [*Chappell et al.*, 1987; *Chappell*, 1988; *Yau and Andre*, 1997; *Cully et al.*, 2003; *Dandouras et al.*, 2005; *Kistler et al.*, 2010; *Liao et al.*, 2010; *Mouikis et al.*, 2010; *Haaland et al.*, 2012b, 2013; *Kronberg et al.*, 2012]. The plasma sheet particles enter the inner magnetosphere on the nightside region, acting to increase the average ion mass for nightside MLT sectors. Therefore, it is expected that the plasma sheet population contributes to the average ion mass distribution, and the convection of plasma sheet ions into the considered region acts to preferentially enhance the average ion mass in the nightside closed magnetosphere.

The distribution of average ion mass along the field lines is modeled using a power law form (equation (2a)), with a negative power law index, β, to represent a maximum in average ion mass at the magnetic equatorial plane, as discussed in section 3. Figure 9a (showing m_{av0} as a function of MLT and L) illustrates the dependences of the empirically modeled equatorial average ion mass parameter, m_{av0}, as defined by equation (2b). The equatorial average ion mass parameter, m_{av0}, (equation (2b)) combines a linear function in L with a sinusoidal component. Equation (2b) shows that the mean value of m_{av0}, averaged over all MLT sectors, decreases linearly with L value. The decrease of the equatorial average ion mass with increased L values is illustrated

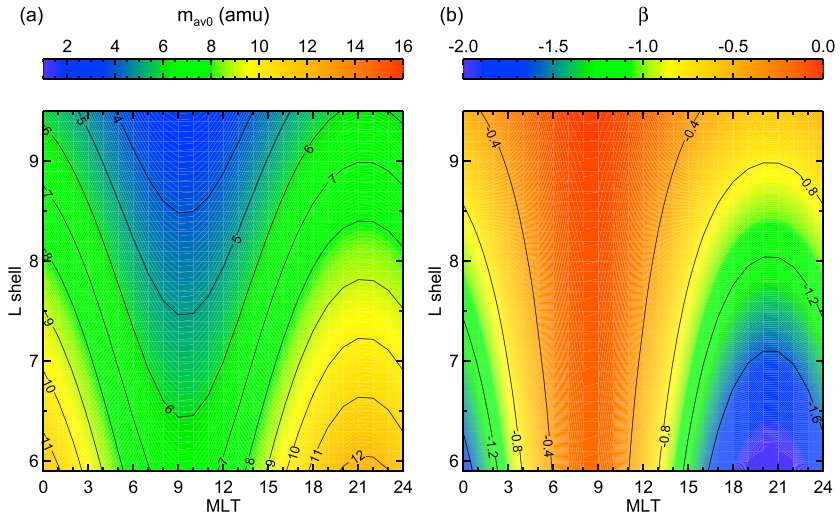

Figure 9. Contour plots showing the variation of the average ion mass model parameters (as defined in equations (2b) and (2c)) with *L* value and MLT.

by Figures 8 and 9a. This feature of the average ion mass distribution is in agreement with previous observations [*Mouikis et al.*, 2010; *Ohtani et al.*, 2011; *Maggiolo and Kistler*, 2014] and is thought to result from the mass dispersion of outflowing ionospheric ions. The heavy ions in the closed magnetosphere predominantly originate from ionospheric outflows at high latitudes. As the plasma is convected into the plasma sheet, mass dispersion occurs, such that low-energy O^+ ions enter the closed magnetosphere at lower *L* values compared to lighter ions [*Lockwood et al.*, 1985; *Chappell*, 1988; *Andre and Yau*, 1997; *Yau and Andre*, 1997; *Haaland et al.*, 2009; *Maggiolo and Kistler*, 2014]. This results in an *L* gradient of O^+ concentration, such that the average ion mass increases toward lower *L* values. Therefore, the observed *L* shell dependence of m_{av0} (see Figure 9a) is a consequence of the plasma sheet properties.

Equation (2b) includes a sinusoidal component for the model parameter m_{av0}, which describes variations of equatorial average ion mass with MLT. Figures 8 and 9a clearly show that the MLT dependence is such that m_{av0} approaches a maximum at approximately 2200 MLT, so the equatorial average ion mass is higher in the evening sector compared to that in the morning sector. This feature can be attributed to plasma sheet convection into the inner magnetosphere. Plasma sheet particles convect into the considered region from the nightside, such that the corresponding average ion mass enhancement will be predominantly localized to nightside MLT sectors.

The function describing the model parameter m_{av0} (equation (2b)) also includes an observed *L* shell dependence for the amplitude of the MLT variation. It can be seen from Figure 9a that the amplitude of the MLT variation decreases with *L* value. As the MLT asymmetry arises as a consequence of heavy ions originating from the plasma sheet, the MLT dependence is expected to be most significant in the region of enhanced heavy ion concentration. This occurs toward the lower *L* values, as previously mentioned.

Equation (2c) defines the power law index, β, which includes a linear function, describing the dependence of the power law index (averaged over all MLT sectors) on *L*, and a sinusoidal component representing the MLT variations. The dependences on *L* and MLT are illustrated in Figure 9b. It can be seen that β linearly becomes less negative for increased *L* values, moving away from the average ion mass enhancement. More negative β values at lower *L* values indicate a steep decrease in average ion mass values away from the magnetic equatorial plane, which is expected to be due to the large enhancement in heavy ions at the magnetic equator due to the effects of the centrifugal force acting on the ions. An additional consideration for decreasing β values with increasing *L* value is the corresponding increase in the flux tube volume and length. Considering ionospheric ions with similar lifetimes, the increased flux tube volume and length means that fewer heavy ions will be concentrated at the magnetic equatorial plane, resulting in flatter distributions along the field line.

The sinusoidal MLT variation of the power law index, β, shown by equation (2c), indicates that the most negative values are located at approximately 2100 MLT, which is clearly shown in Figure 9b. This is due to a

decreased upwelling of ionospheric O^+ ions on the nightside field lines, as a result of reduced photoionization from solar radiation [*Young et al.*, 1982; *Lennartsson*, 1989; *Stokholm et al.*, 1989]. This causes the values to decrease more rapidly from the equatorial enhancement toward the ionospheric ends for nightside field lines, thus causing a steeper distribution along the field line, represented by a more negative power law index.

Furthermore, the plasma sheet contribution acts to increase the gradient along nightside field lines, relative to the dayside. As previously discussed, the average ion mass enhancement due to this feature is greatest for nightside MLT sectors compared to the dayside (see Figures 8 and 9a). The increase in the relative concentration of heavy ions in the equatorial region of flux tubes in the nightside region corresponds to an increased gradient in average ion mass along the field line. The result is a more negative power law index, β, value on nightside field lines than dayside field lines, where the average ion mass is reduced.

The discussion of the average ion mass distribution has mainly focused on the contribution of the plasma sheet population, which is convected into the closed magnetosphere. However, an additional source of heavy ions, which will influence the average ion mass of the plasma in this region, is the heavy ion torus. The heavy ion torus is a region of enhanced O^+ densities located just outside the plasmasphere, with no corresponding enhancement for the densities of light ions [*Chappell*, 1982; *Horwitz et al.*, 1984, 1986; *Roberts et al.*, 1987; *Comfort et al.*, 1988; *Berube et al.*, 2005; *Darrouzet et al.*, 2009; *Nosé et al.*, 2011, 2015]. The increased O^+ concentration will clearly correspond to an increase in the average ion mass of the plasma in the heavy ion torus. The expected L value position of the heavy ion torus typically ranges from $L \sim 4.5$ to 6.5 [*Nosé et al.*, 2011], with decreasing heavy ion enhancements, indicating the outer edge of the torus, observed at $L \sim 6–8$ [*Lee and Angelopoulos*, 2014]. It has been proposed that the heavy ion torus is the result of the interaction between the plasmasphere and the ring current [*Horwitz et al.*, 1986; *Roberts et al.*, 1987; *Nosé et al.*, 2011]. This interaction is expected to be most intense in the evening region, just beyond the duskside bulge region [*Roberts et al.*, 1987; *Burch et al.*, 2001]. As only the outer edge of the heavy ion torus coincides with the L range considered by this study, it is expected that the heavy ion torus contribution is minor in comparison with the plasma sheet contribution for this region. Nevertheless, the heavy ion torus acts to increase the average ion mass at lower L values in the dusk MLT sectors, further intensifying the average ion mass enhancement, which is shown in Figure 8.

5. Conclusions and Further Work

This study has obtained an empirical model describing the distribution of average ion mass along closed geomagnetic field lines, including dependences with L shell and MLT. This involved using observations obtained by the CODIF instrument on board Cluster, for a time interval spanning approximately 2001–2005, between $5.9 \leq L < 9.5$. A key result obtained is the inclusion of the observed enhancement of heavy ions, located at low L values in the evening MLT sector, expected to originate from high-latitude ionospheric outflows, in the average ion mass model. The resulting model provides an important insight into the heavy ion loading processes occurring in this region and their dependences on L and MLT. Notable differences between this model and previous empirical models are the size and coverage of the underlying data sets and that variations along the field lines have been considered, as opposed to only considering equatorial variations.

This study is to be supplemented further by examining variations in the spatial distribution of average ion mass with different parameters and indices, quantifying solar wind and geomagnetic activity dependences [*Young et al.*, 1982; *Kistler et al.*, 2010; *Mouikis et al.*, 2010; *Ohtani et al.*, 2011; *Kronberg et al.*, 2012; *Ozhogin et al.*, 2012; *Maggiolo and Kistler*, 2014; *Maes et al.*, 2015]. This will provide information on the processes occurring with varying conditions and how they influence the resulting average ion mass distribution in the closed magnetosphere.

An area of future work involves determining a corresponding empirical model describing the total electron density distribution along closed geomagnetic field lines. By combining the model with the empirical average ion mass model presented here, the total plasma mass density spatial distribution can be estimated for the region considered. This is a key motivation, as variations in the total plasma mass density provide information on the morphology and dynamics of the magnetosphere, and has significant implications for a variety of magnetospheric processes (e.g., propagation of wave modes implicated in radiation belt energization and decay, and magnetic reconnection rates).

Acknowledgments
J.K.S. is supported by STFC studentship ST/K502121, T.K.Y. is supported by STFC grant ST/H002480/1, and R.C.F. is supported by STFC Ernest Rutherford Fellowship ST/K004298/1. The authors would like to thank the CIS PI and instrument team and the CSA (http://www.cosmos.esa.int/web/csa) for providing the Cluster data used. French participation in the Cluster project is funded by CNES. We also thank the referees for their constructive comments. OMNI data were obtained from the NASA/GSFC OMNIWeb interface (http://omniweb.gsfc.nasa.gov). The *Dst* index data were obtained from the World Data Center for Geomagnetism, Kyoto (http://wdc.kugi.kyoto-u.ac.jp/dstae/index.html). The data underlying this study are freely available from the above archives. The analysis code used in this study is stored on University of Leicester computer systems and is available on request.

References

Andre, M., and A. Yau (1997), Theories and observations of ion energization and outflow in the high latitude magnetosphere, *Space Sci. Rev.*, *80*, 27–48, doi:10.1023/A:1004921619885.

Berube, D., M. B. Moldwin, S. F. Fung, and J. L. Green (2005), A plasmaspheric mass density model and constraints on its heavy ion concentration, *J. Geophys. Res.*, *110*, A04212, doi:10.1029/2004JA010684.

Borovsky, J. E., and M. H. Denton (2006), Effect of plasmaspheric drainage plumes on solar-wind/magnetosphere coupling, *Geophys. Res. Lett.*, *33*, L20101, doi:10.1029/2006GL026519.

Burch, J. L., D. G. Mitchell, B. R. Sandel, P. C. Brandt, and M. Wüest (2001), Global dynamics of the plasmasphere and ring current during magnetic storms, *Geophys. Res. Lett.*, *28*, 1159–1162, doi:10.1029/2000GL012413.

Chappell, C. R. (1982), Initial observations of thermal plasma composition and energetics from Dynamics Explorer-1, *Geophys. Res. Lett.*, *9*, 929–932, doi:10.1029/GL009i009p00929.

Chappell, C. R. (1988), The terrestrial plasma source—A new perspective in solar-terrestrial processes from Dynamics Explorer, *Rev. Geophys.*, *26*, 229–248, doi:10.1029/RG026i002p00229.

Chappell, C. R., T. E. Moore, and J. H. Waite Jr. (1987), The ionosphere as a fully adequate source of plasma for the Earth's magnetosphere, *J. Geophys. Res.*, *92*, 5896–5910, doi:10.1029/JA092iA06p05896.

Clark, J., and A. Gelfand (2006), *Hierarchical Modelling for the Environmental Sciences: Statistical Methods and Applications, Oxford Biol.*, Oxford Univ. Press, Oxford, U. K.

Clausen, L. B. N., T. K. Yeoman, R. C. Fear, R. Behlke, E. A. Lucek, and M. J. Engebretson (2009), First simultaneous measurements of waves generated at the bow shock in the solar wind, the magnetosphere and on the ground, *Ann. Geophys.*, *27*, 357–371, doi:10.5194/angeo-27-357-2009.

Comfort, R. H., I. T. Newberry, and C. R. Chappell (1988), Preliminary statistical survey of plasmaspheric ion properties from observations by DE 1/RIMS, in *Modeling Magnetospheric Plasma, Geophys. Monogr. Ser.*, vol. 44, edited by T. E. Moore et al., pp. 107–114, AGU, Washington, D. C., doi:10.1029/GM044p0107

Cully, C. M., E. F. Donovan, A. W. Yau, and H. J. Opgenoorth (2003), Supply of thermal ionospheric ions to the central plasma sheet, *J. Geophys. Res.*, *108*(A2), 1092, doi:10.1029/2002JA009457.

Dandouras, I., et al. (2005), Multipoint observations of ionic structures in the plasmasphere by CLUSTER–CIS and comparisons with IMAGE-EUV observations and with model simulations, in *Inner Magnetosphere Interactions: New Perspectives From Imaging, Geophys. Monogr. Ser.*, vol. 159, edited by J. Burch, M. Schulz, and H. Spence, pp. 23–53, AGU, Washington, D. C.

Dandouras, I., J. Cao, and C. Vallat (2009), Energetic ion dynamics of the inner magnetosphere revealed in coordinated Cluster-Double Star observations, *J. Geophys. Res.*, *114*, A01S90, doi:10.1029/2007JA012757.

Darrouzet, F., et al. (2009), Plasmaspheric density structures and dynamics: Properties observed by the CLUSTER and IMAGE missions, *Space Sci. Rev.*, *145*, 55–106, doi:10.1007/s11214-008-9438-9.

Denton, R. E., K. Takahashi, I. A. Galkin, P. A. Nsumei, X. Huang, B. W. Reinisch, R. R. Anderson, M. K. Sleeper, and W. J. Hughes (2006), Distribution of density along magnetospheric field lines, *J. Geophys. Res.*, *111*, A04213, doi:10.1029/2005JA011414.

Denton, R. E., P. M. E. Décréau, M. J. Engebretson, F. Darrouzet, and J. L. Posch (2009), Field line distribution of density at $L = 4.8$ inferred from observations by CLUSTER, *Ann. Geophys.*, *27*, 705–724, doi:10.5194/angeo-27-705-2009.

Escoubet, C. P., R. Schmidt, and M. L. Goldstein (1997), Cluster—Science and mission overview, *Space Sci. Rev.*, *79*, 11–32, doi:10.1023/A:1004923124586.

Ganushkina, N. Y., I. Dandouras, Y. Y. Shprits, and J. Cao (2011), Locations of boundaries of outer and inner radiation belts as observed by Cluster and Double Star, *J. Geophys. Res.*, *116*, A09234, doi:10.1029/2010JA016376.

Haaland, S., B. Lybekk, K. Svenes, A. Pedersen, M. Förster, H. Vaith, and R. Torbert (2009), Plasma transport in the magnetotail lobes, *Ann. Geophys.*, *27*, 3577–3590, doi:10.5194/angeo-27-3577-2009.

Haaland, S., K. Svenes, B. Lybekk, and A. Pedersen (2012a), A survey of the polar cap density based on Cluster EFW probe measurements: Solar wind and solar irradiation dependence, *J. Geophys. Res.*, *117*, A01216, doi:10.1029/2011JA017250.

Haaland, S., et al. (2012b), Estimating the capture and loss of cold plasma from ionospheric outflow, *J. Geophys. Res.*, *117*, A07311, doi:10.1029/2012JA017679.

Haaland, S. et al. (2013), Cold ion outflow as a source of plasma for the magnetosphere, in *Dynamics of the Earth's Radiation Belts and Inner Magnetosphere*, pp. 341–354, AGU, Washington, D. C., doi:10.1029/2012GM001317

Horwitz, J. L., R. H. Comfort, and C. R. Chappell (1984), Thermal ion composition measurements of the formation of the new outer plasmasphere and double plasmapause during storm recovery phase, *Geophys. Res. Lett.*, *11*, 701–704, doi:10.1029/GL011i008p00701.

Horwitz, J. L., R. H. Comfort, L. H. Brace, and C. R. Chappell (1986), Dual-spacecraft measurements of plasmasphere-ionosphere coupling, *J. Geophys. Res.*, *91*, 11,203–11,216, doi:10.1029/JA091iA10p11203.

Howarth, A., and A. W. Yau (2008), The effects of IMF and convection on thermal ion outflow in magnetosphere-ionosphere coupling, *J. Atmos. Sol. Terr. Phys.*, *70*, 2132–2143, doi:10.1016/j.jastp.2008.08.008.

Kistler, L. M., et al. (2006), Ion composition and pressure changes in storm time and nonstorm substorms in the vicinity of the near-Earth neutral line, *J. Geophys. Res.*, *111*, A11222, doi:10.1029/2006JA011939.

Kistler, L. M., C. G. Mouikis, B. Klecker, and I. Dandouras (2010), Cusp as a source for oxygen in the plasma sheet during geomagnetic storms, *J. Geophys. Res.*, *115*, A03209, doi:10.1029/2009JA014838.

Korth, A., R. H. W. Friedel, F. Frutos-Alfaro, C. G. Mouikis, and Q. Zong (2002), Ion composition of substorms during storm-time and non-storm-time periods, *J. Atmos. Sol. Terr. Phys.*, *64*, 561–566, doi:10.1016/S1364-6826(02)00013-5.

Kronberg, E. A., S. E. Haaland, P. W. Daly, E. E. Grigorenko, L. M. Kistler, M. Fränz, and I. Dandouras (2012), Oxygen and hydrogen ion abundance in the near-Earth magnetosphere: Statistical results on the response to the geomagnetic and solar wind activity conditions, *J. Geophys. Res.*, *117*, A12208, doi:10.1029/2012JA018071.

Lee, J. H., and V. Angelopoulos (2014), On the presence and properties of cold ions near Earth's equatorial magnetosphere, *J. Geophys. Res. Space Physics*, *119*, 1749–1770, doi:10.1002/2013JA019305.

Lemaire, J. F., and K. I. Gringauz (1998), *The Earth's Plasmasphere*, Cambridge Univ. Press, Cambridge, U. K.

Lennartsson, W. (1989), Energetic (0.1- to 16- keV/e) magnetospheric ion composition at different levels of solar $F_{10.7}$, *J. Geophys. Res.*, *94*, 3600–3610, doi:10.1029/JA094iA04p03600.

Li, K., et al. (2012), On the ionospheric source region of cold ion outflow, *Geophys. Res. Lett.*, *39*, L18102, doi:10.1029/2012GL053297.

Liao, J., L. M. Kistler, C. G. Mouikis, B. Klecker, I. Dandouras, and J.-C. Zhang (2010), Statistical study of O^+ transport from the cusp to the lobes with Cluster CODIF data, *J. Geophys. Res.*, *115*, A00J15, doi:10.1029/2010JA015613.

Lockwood, M., J. H. Waite Jr., T. E. Moore, C. R. Chappell, and M. O. Chandler (1985), The cleft ion fountain, *J. Geophys. Res.*, *90*, 9736–9748, doi:10.1029/JA090iA10p09736.

Maes, L., R. Maggiolo, J. De Keyser, I. Dandouras, R. C. Fear, D. Fontaine, and S. Haaland (2015), Solar illumination control of ionospheric outflow above polar cap arcs, *Geophys. Res. Lett.*, *42*, 1304–1311, doi:10.1002/2014GL062972.

Maggiolo, R., and L. M. Kistler (2014), Spatial variation in the plasma sheet composition: Dependence on geomagnetic and solar activity, *J. Geophys. Res. Space Physics*, *119*, 2836–2857, doi:10.1002/2013JA019517.

Meredith, N. P., R. M. Thorne, R. B. Horne, D. Summers, B. J. Fraser, and R. R. Anderson (2003), Statistical analysis of relativistic electron energies for cyclotron resonance with EMIC waves observed on CRRES, *J. Geophys. Res.*, *108*(A6), 1250, doi:10.1029/2002JA009700.

Moore, T. E., et al. (1999), Polar/TIDE results on polar ion outflows, in *Sun-Earth Plasma Connections, Geophys. Monogr. Ser.*, vol. 109, edited by J. L. Burch, R. L. Carovillano, and S. K. Antiochos, pp. 87–101, AGU, Washington, D. C., doi:10.1029/GM109p0087

Mouikis, C. G., L. M. Kistler, Y. H. Liu, B. Klecker, A. Korth, and I. Dandouras (2010), H^+ and O^+ content of the plasma sheet at 15–19 *Re* as a function of geomagnetic and solar activity, *J. Geophys. Res.*, *115*, A00J16, doi:10.1029/2010JA015978.

Mouikis, C. G., L. M. Kistler, G. Wang, and Y. Liu (2014), Background subtraction for the Cluster/CODIF plasma ion mass spectrometer, *Geosci. Instrum. Methods Data Sys.*, *3*, 41–48, doi:10.5194/gi-3-41-2014.

Nosé, M., K. Takahashi, R. R. Anderson, and H. J. Singer (2011), Oxygen torus in the deep inner magnetosphere and its contribution to recurrent process of O^+-rich ring current formation, *J. Geophys. Res.*, *116*, A10224, doi:10.1029/2011JA016651.

Nosé, M., et al. (2015), Formation of the oxygen torus in the inner magnetosphere: Van Allen Probes observations, *J. Geophys. Res. Space Physics*, *120*, 1182–1196, doi:10.1002/2014JA020593.

O'Brien, T. P., K. R. Lorentzen, I. R. Mann, N. P. Meredith, J. B. Blake, J. F. Fennell, M. D. Looper, D. K. Milling, and R. R. Anderson (2003), Energization of relativistic electrons in the presence of ULF power and MeV microbursts: Evidence for dual ULF and VLF acceleration, *J. Geophys. Res.*, *108*(A8), 1329, doi:10.1029/2002JA009784.

Ohtani, S., M. Nosé, S. P. Christon, and A. T. Y. Lui (2011), Energetic O^+ and H^+ ions in the plasma sheet: Implications for the transport of ionospheric ions, *J. Geophys. Res.*, *116*, A10211, doi:10.1029/2011JA016532.

Ozhogin, P., J. Tu, P. Song, and B. W. Reinisch (2012), Field-aligned distribution of the plasmaspheric electron density: An empirical model derived from the IMAGE RPI measurements, *J. Geophys. Res.*, *117*, A06225, doi:10.1029/2011JA017330.

Peterson, W. K., L. Andersson, B. C. Callahan, H. L. Collin, J. D. Scudder, and A. W. Yau (2008), Solar-minimum quiet time ion energization and outflow in dynamic boundary related coordinates, *J. Geophys. Res.*, *113*, A07222, doi:10.1029/2008JA013059.

Rème, H., et al. (1997), The Cluster Ion Spectrometry (CIS) experiment, *Space Sci. Rev.*, *79*, 303–350, doi:10.1023/A:1004929816409.

Roberts, W. T., Jr., J. L. Horwitz, R. H. Comfort, C. R. Chappell, J. H. Waite Jr., and J. L. Green (1987), Heavy ion density enhancements in the outer plasmasphere, *J. Geophys. Res.*, *92*, 13,499–13,512, doi:10.1029/JA092iA12p13499.

Seki, K., M. Hirahara, M. Hoshino, T. Terasawa, R. C. Elphic, Y. Saito, T. Mukai, H. Hayakawa, H. Kojima, and H. Matsumoto (2003), Cold ions in the hot plasma sheet of Earth's magnetotail, *Nature*, *422*, 589–592.

Shelley, E. G., R. G. Johnson, and R. D. Sharp (1972), Satellite observations of energetic heavy ions during a geomagnetic storm, *J. Geophys. Res.*, *77*, 6104–6110, doi:10.1029/JA077i031p06104.

Shelley, E. G., W. K. Peterson, A. G. Ghielmetti, and J. Geiss (1982), The polar ionosphere as a source of energetic magnetospheric plasma, *Geophys. Res. Lett.*, *9*, 941–944, doi:10.1029/GL009i009p00941.

Slapak, R., H. Nilsson, L. G. Westerberg, and A. Eriksson (2012), Observations of oxygen ions in the dayside magnetosheath associated with southward IMF, *J. Geophys. Res.*, *117*, A07218, doi:10.1029/2012JA017754.

Stokholm, M., H. Balsiger, J. Geiss, H. Rosenbauer, and D. T. Young (1989), Variations of the magnetospheric ion number densities near geostationary orbit with solar activity, *Ann. Geophys.*, *7*, 69–75.

Tabachnick, B. G., and L. S. Fidell (2006), *Using Multivariate Statistics* 5th ed., Allyn and Bacon, Needham Height, Mass.

Takahashi, K., R. E. Denton, R. R. Anderson, and W. J. Hughes (2004), Frequencies of standing Alfvén wave harmonics and their implication for plasma mass distribution along geomagnetic field lines: Statistical analysis of CRRES data, *J. Geophys. Res.*, *109*, A08202, doi:10.1029/2003JA010345.

Tsyganenko, N. A. (1996), Effects of the solar wind conditions in the global magnetospheric configurations as deduced from data-based field models (Invited), in *Proceedings of the 3rd International Conference on Substorms, Versailles, 12–17 May, ESA Spec. Publ.*, vol. 389, edited by E. J. Rolfe and B. Kaldeich, pp. 181–186, Eur. Space Agency, Paris.

Winglee, R. M. (2000), Mapping of ionospheric outflows into the magnetosphere for varying IMF conditions, *J. Atmos. Sol. Terr. Phys.*, *62*, 527–540, doi:10.1016/S1364-6826(00)00015-8.

Yamauchi, M., I. Dandouras, H. Rème, and H. Nilsson (2014a), Cluster observations of hot He^+ events in the inner magnetosphere, *J. Geophys. Res. Space Physics*, *119*, 2706–2716, doi:10.1002/2013JA019724.

Yamauchi, M., Y. Ebihara, H. Nilsson, and I. Dandouras (2014b), Ion drift simulation of sudden appearance of sub- keV structured ions in the inner magnetosphere, *Ann. Geophys.*, *32*, 83–90, doi:10.5194/angeo-32-83-2014.

Yau, A. W., and M. Andre (1997), Sources of ion outflow in the high latitude ionosphere, *Space Sci. Rev.*, *80*, 1–25, doi:10.1023/A:1004947203046.

Young, D. T., H. Balsiger, and J. Geiss (1982), Correlations of magnetospheric ion composition with geomagnetic and solar activity, *J. Geophys. Res.*, *87*, 9077–9096, doi:10.1029/JA087iA11p09077.

Erratum

In the originally published version of this article, the top panel of Figure 4 (an energy-spectrogram) was mistakenly inverted, which results in incorrect energies attributed to the line plots shown in the second, third, and fourth panels of Figure 4. Panel 5 in Figure 4 was also wrongly drawn, due to an incorrect choice of coordinate system. Both panels of the figure have since been corrected, and this version may be considered the version of record.